Fermi National Accelerator Laboratory

FERMILAB-Conf-98/268-E
D0

The D0 Detector Upgrade and Jet Energy Scale

Maria Teresa Roco
For the D0 Collaboration

Fermi National Accelerator Laboratory
P.O. Box 500, Batavia, Illinois 60510

September 1998

Published Proceedings of the *XXIX International Conference on High Energy Physics 1998*, Vancouver, B.C. Canada, July 23-29, 1998

Operated by Universities Research Association Inc. under Contract No. DE-AC02-76CH03000 with the United States Department of Energy

Disclaimer

Distribution

THE DØ DETECTOR UPGRADE AND JET ENERGY SCALE

MARIA TERESA ROCO
For the DØ Collaboration

MS 357 Fermilab, P.O. Box 500, Batavia, IL. 60510-0500, U.S.A.
E-mail: roco@fnal.gov

A major detector upgrade project is presently underway for the DØ experiment in preparation for Run 2 of the Fermilab Tevatron collider scheduled to begin in the year 2000. The upgrade is driven by the DØ Run 2 physics goals and by the higher event rates and backgrounds expected in the new high luminosity environment. A general overview of the DØ upgrade is given in the first part of this report. The second part describes the calibration of jets observed with the DØ detector at the transverse energy and pseudorapidity range $E_T > 8\ GeV$ and $|\eta| < 3$.

1 The DØ Detector Upgrade

The Fermilab Tevatron collider luminosity upgrade program involves the replacement of the existing Main Ring accelerator with the Main Injector and the construction of a new antiproton storage ring within a common tunnel. The ultimate performance goal of the collider upgrade for Run 2 is to achieve luminosities up to $2 \times 10^{32} cm^{-2} s^{-1}$, more than an order of magnitude increase over the previous run. In addition, the center-of-mass energy will increase to $2\ TeV$ and the bunch spacing will be reduced to 396 ns and eventually to 132 ns, substantially shorter than 3.5 μs in Run 1.

The higher luminosities and much shorter bunch crossing time require some major modifications to the DØ detector to optimize its physics capabilities in the new Main Injector era. A major element of the detector upgrade [1] involves the replacement of the inner tracking systems and the installation of a 2 Tesla superconducting solenoid. The new tracking system includes a scintillating fiber tracker, a silicon vertex detector and preshower detectors in the central and forward regions. Improvements to the muon detector are required to handle the higher event rates and backgrounds expected in Run 2. These include the installation of fast trigger elements and the addition of shielding material to reduce the detector occupancy. Electronic upgrades are necessary to handle the smaller bunch spacing and to provide pipelining for the front-end signals coming from the calorimeter, muon and tracking systems. A sophisticated trigger control system is planned to integrate the new detector trigger elements and front-end electronics, and to reduce the raw event rates to a manageable level.

1.1 Tracking System

The momenta of charged particles are determined from their curvature in the uniform 2 Tesla axial magnetic field provided by a superconducting solenoid. The 2.8 m long solenoid has a two layer coil with a mean radius of 60 cm. It encloses the scintillating fiber tracker and the silicon microstrip vertex detector. The fiber tracker provides charged particle track reconstruction, momentum measurement within $|\eta| < 2$ and a fast first level track triggering with good resolution. It consists of eight concentric barrels of scintillating fiber doublet layers, one layer with fibers parallel to the beam line and another layer with $\pm 2^o$ stereo. It has an active length of 2.6 m and a radial coverage 20 $cm < r < 50\ cm$. There are approximately 77,000 fibers which are connected to the photodetectors via 11 m long clear waveguides. The optical signals from the fibers are detected by visible photon light counters (VLPC). VLPCs are arsenic-doped silicon diodes which operate at temperatures between 8-10 ^oK. A large sample of the VLPCs were tested in a cosmic ray test stand [2]. The sample exhibited $\sim 80\%$ quantum efficiency, relatively high gain and less than 0.1% noise occupancy when operated at full efficiency. The doublet hit efficiency for cosmic ray tracks is better than 99.9% and a position resolution $\sim 100 \mu m$ is obtained.

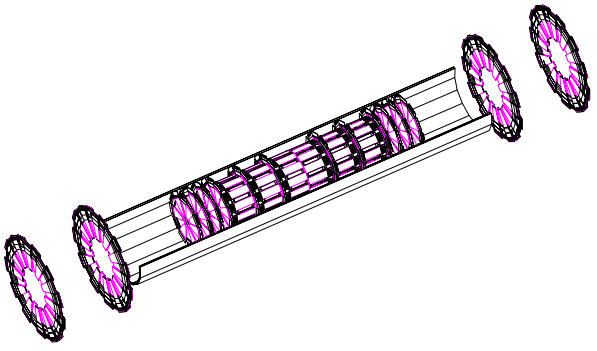

Figure 1: The silicon microstrip tracker consists of disks interspersed with barrels.

The main factors which constrain the design of the silicon microstrip tracker include [3]: the extended luminous region in z, three dimensional track reconstruction capabilities with transverse impact parameter resolutions better than 30 μm, radiation hardness to cope with the

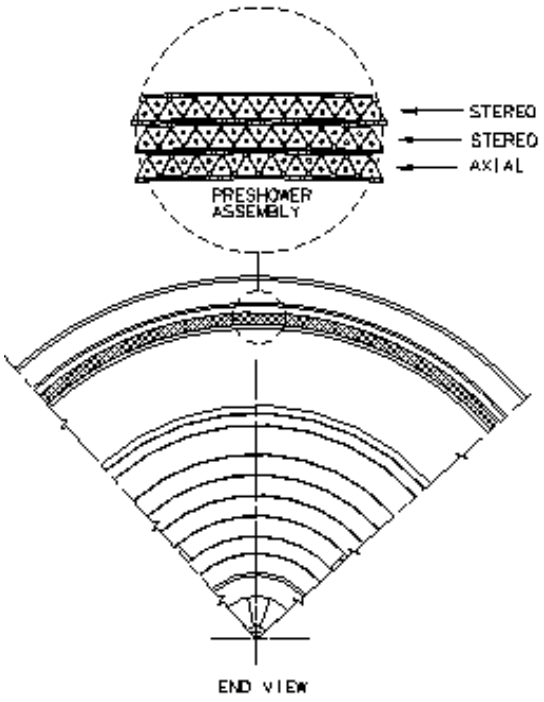

Figure 2: Cross sectional end view of the tracking system showing the central preshower assembly.

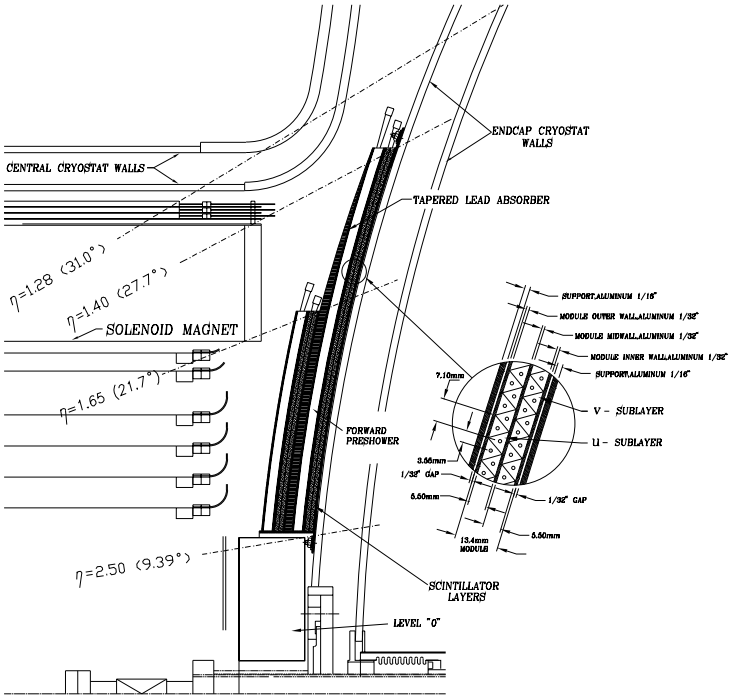

Figure 3: Side view of the tracking system showing the forward preshower assembly.

expected Run 2 delivered luminosity of 2-5 fb^{-1}, and electronics and readout which can operate reliably with bunch crossing intervals down to 132 ns. The long luminous region sets the length scale and motivates a hybrid design which consists of disk and barrel modules shown in Fig. 1. Larger disks at $z = \pm 94\ cm, \pm 126\ cm$ provide improved momentum resolution up to $\eta = \pm 3$. The barrel and disk modules are supported by a double-walled carbon-fiber/epoxy half cylinder which aids in maintaining the precise relative alignment and supports the detector cabling and cooling services. Each barrel contains four concentric layers of silicon detectors ranging from 2.6 cm to 10 cm. The basic detector unit is the ladder, which consists of two 300 μm thick wafers, 6 cm × 2.1 cm, positioned end to end and electrically connected by microwirebonds. The wafers are held in position by two longitudinal rails consisting of Rohacell foam and carbon fiber sandwich. Four inner barrels around $z = 0$ have layers of double-sided silicon ladders with either a 2^o or 90^o stereo angle. The outer barrels have single-sided ladders in layers 1,3 while layers 2,4 are double-sided with 2^o stereo. The ladders are supported by beryllium bulkheads with very tight tolerances since they establish the precision of the alignment. By means of an integrated coolant channel, the bulkheads also provide cooling for the electrical components mounted at one end of the ladder. To avoid excessive radiation damage, the detectors are operated at temperatures between 5-10 ^oC. The ladders, as well as the fiber tracker VLPC system, are read out by radiation hard CMOS custom integrated circuits, SVX-IIe chips [4], optimized for 396 ns and 132 ns bunch crossing intervals. This new 128 channel device incorporates preamplifiers, 32 cell analog pipelines, 8 bit ADCs, and sparsification. The SVX-II chip is highly flexible, with programmable test pulse patterns, ADC ramp, pedestal, bandwidth and polarity.

The cylindrical central preshower detector, shown in Fig. 2, is designed to enhance the identification of electrons and photons, provide precise position measurements in the region $|\eta| < 1.2$, and correct the calorimeter electromagnetic energy for the effects of the solenoid. It is installed in the small gap between the solenoid coil and the central calorimeter cryostat at a radius of 72 cm. It consists of three layers of 7 mm base triangular scintillating strips with wavelength-shifting fiber readout. The fast energy and position measurements enable the use of the preshower information at the trigger level. Simulation studies show that the central preshower information allows the electron trigger rate to be reduced by a factor of 3-5 without a loss in efficiency. There are also forward preshower detectors, shown in Fig. 3, mounted on the face of each end calorimeter cryostat. Like the central preshower detector, they are intended to improve the electron identification and triggering capabilities by making precise position measurements of particle trajectories using dE/dx and showering information.

1.2 *Muon Detector*

The upgraded muon system is designed to provide excellent muon identification and muon triggering capabilities for $|\eta| < 2$. For $|\eta| < 1$, the existing proportional drift tubes (PDT) are retained and a faster gas mixture is used to reduce the drift time from 750 ns to 450 ns. The front-end electronics are replaced to allow a deadtimeless operation. A new layer of scintillation counters are installed between the calorimeter and the inner PDT layer. They are used, together with the fiber tracker information, to reject out-of-time backgrounds and to enable a reduced trigger threshold for low p_T muons down to 2 GeV/c. For the forward muon system covering $1 < |\eta| < 2$, the PDTs are replaced with planes of plastic mini-drift tubes (MDTs). Three layers of scintillator pixel counters, shown in Fig. 4, provide time information and matching of muon tracks with the fiber tracker. The minimum pixel size, $\Delta\eta = 0.1$ and $\Delta\phi = 4.5^o$, is dictated by the requirement of efficient muon identification and triggering down to $p_T = 3\ GeV/c$. The muon detector upgrade also includes the addition of shielding material extending from the rear of the calorimeter to the accelerator tunnel to substantially reduce the background arising from the scattered beam fragments exiting the calorimeter and the beam pipe.

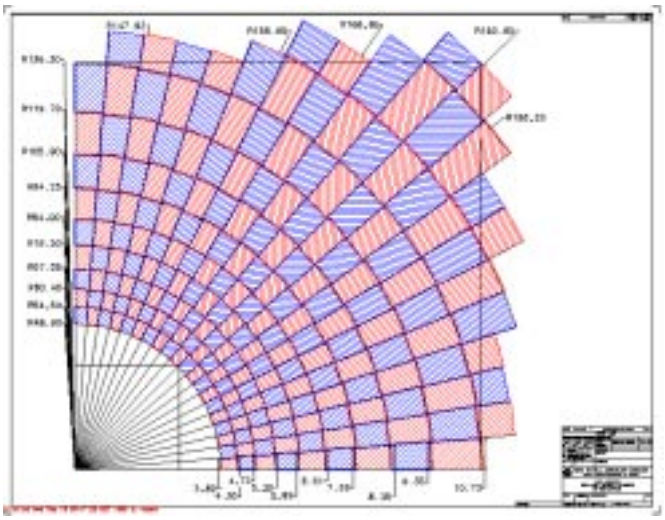

Figure 4: One quadrant of a forward muon scintillation pixel plane.

1.3 *Trigger and Data Acquisition Systems*

A new trigger system is designed to deal with the higher event rates in Run 2. The system includes three hardware trigger levels, $L0, L1$, $L2$, and a software trigger $L3$. $L0$, which serves primarily as a luminosity monitor, provides an inelastic collision trigger. $L1$ reduces

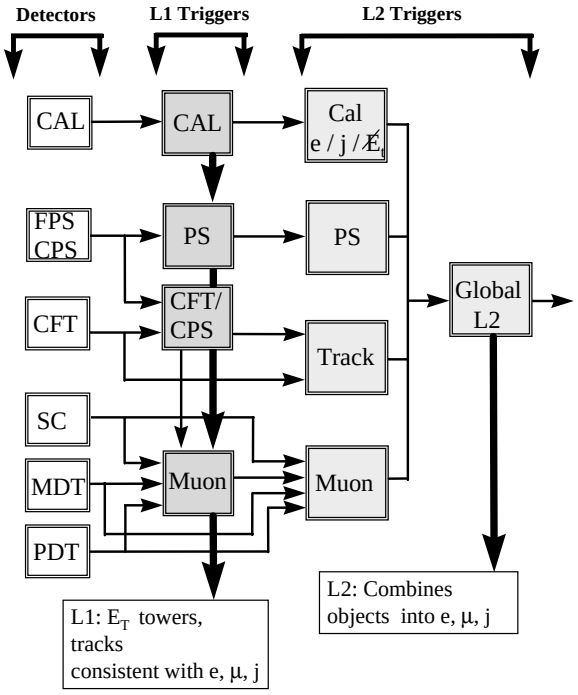

Figure 5: $L1$ and $L2$ block diagram.

the inelastic trigger rate by a factor of 10^3 while maintaining a high trigger acceptance for leptons and jets. Fig. 5 shows the $L1$ and $L2$ block diagram. The new $L1$ trigger includes the calorimeter, central fiber tracker (CFT), central (CPS) and forward preshower (FPS) detectors, muon scintillation counters and chambers. For deadtimeless operation, all $L1$ triggers are pipelined and buffered. $L1$ provides a trigger decision in 4.2 μs and has an accept rate of 5-10 KHz. The number of triggers at $L1$ is 128 and fractional prescales may be available. The $L2$ system consists of a set of detector-specific preprocessors which prepare the information to be sent to the global processors. The result of the preprocessing algorithm is a list of candidate objects from each detector such as muons, electrons, jets, tracks and secondary vertices. The $L2$ system introduces a minimal amount of deadtime ($< 1\%$). It makes a trigger decision within 400 μs with an accept rate of 1 KHz, providing a rejection factor of 10. The $L3$ trigger system uses a farm of standard high-performance commercial processors to run event filtering algorithms. $L3$ makes a trigger decision in 100 ms and the accept rate is 20-50 Hz.

The data acquisition system is basically unchanged from Run 1. The architecture has been designed with parallel and redundant paths which provide a high degree of reliability in case of a component failure. VME buffer drivers (VBD) drive the raw data via high-speed data cables which feed a new data distributor system where

further buffering is performed. The data is passed to a farm of event building and filtering $L3$ processing nodes. Its output goes to another VBD and data cable system which feeds the data to a host interface node. This node transfers the data to data-logging and monitoring cluster nodes via a standard network connection. Event reconstruction is performed on the Fermilab processor farm system capable of matching the 20-50 Hz data acquisition rate. Processed data are then stored on a robotic tape system and made available for analysis. In Run 2 the expected nominal event size is roughly 250 KBytes.

1.4 Calorimeter Upgrade

To maintain the excellent performance of the calorimeter for running conditions expected in Run 2, an upgrade of the calorimeter system is required. The uranium liquid-argon calorimeter remains unchanged but modifications to the front-end electronics are necessary. The shorter bunch spacing and high luminosity conditions require a re-optimization of the noise arising from the electronics, pile-up and uranium radioactivity. This can be achieved by shortening the effective integration time and reducing the intrinsic noise of the preamplifier. Pile-up effects in the calorimeter are minimized by reducing the peak sampling time from 2.2 μs to 400 ns. The increased sensitivity to noise and signal reflections in the signal cables due to the shorter shaping times require new preamplifier hybrids as well as impedance matched cables which have better noise performance. Switched capacitor arrays perform the necessary pipelining of the calorimeter signals to provide time to generate a trigger decision.

2 The Jet Energy Scale in the DØ Calorimeters

The major source of systematic uncertainty in both the DØ inclusive jet cross section and top quark mass measurements is the jet energy scale. The calorimeters[5] are the primary tool for jet measurements at DØ. An accurate understanding of the calorimeter energy calibration is essential since most physics measurements at the Tevatron involve events with jets. After a brief summary of the characteristics and performance of the DØ calorimeters, the different corrections involved in the jet energy calibration are enumerated below[6].

2.1 DØ Calorimeters

The DØ experiment has a hermetic, finely-segmented, thick, radiation-hard calorimeter based on the detection of ionization in liquid argon. The central (CC) and end (EC) sections, shown in Fig. 6, contain approximately 7 and 8 interaction lengths of material, ensuring the containment of nearly all particles except neutrinos and high p_T muons. The hermetic calorimeter consists of plates of depleted uranium in the electromagnetic (EM) and fine hadronic (FH) sections, and either copper or stainless steel in the coarse hadronic (CH) sections. The segmentation is $\Delta\eta \times \Delta\phi = 0.1 \times 0.1$ (0.05×0.05 at the EM shower maximum).

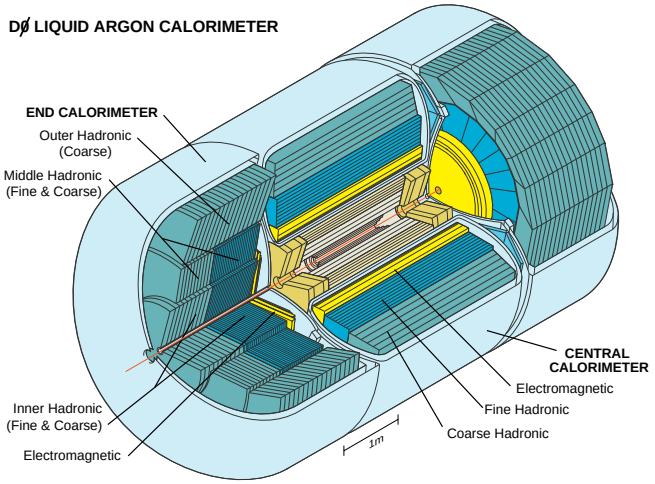

Figure 6: View of the DØ calorimeters.

From previous test beam measurements[7], the energy resolution for single electrons and pions, with energy E in GeV, are given by $\sigma(E)/E \sim 15\%/\sqrt{E}$ and $50\%/\sqrt{E}$, respectively. The DØ calorimeters are nearly compensating with e/π ratio less than 1.05 above 30 GeV.

2.2 Jet Energy Calibration

Jet energies measured in the calorimeter are distorted by particle energy losses in the material in front of the calorimeter, detector noise, phenomena which affect the response such as detector boundaries, non-uniformities and e/π, and jet reconstruction and resolution effects. The goal of the jet energy calibration is to obtain the particle-level or true jet energy from the observed jet energy measured in the calorimeter. Energy corrections are derived using the reconstructed Run 1 data sets at center-of-mass energies 1800 GeV and 630 GeV. A fixed cone algorithm is used to reconstruct jets from cell energy depositions in the calorimeter. The particle level jet energy, E_{jet}^{ptcl}, is obtained from

$$E_{jet}^{ptcl} = \frac{E_{jet}^{meas} - E_O}{R_{jet} \cdot S}. \quad (1)$$

E_O is an offset correction. It subtracts the excess energy not associated with the high p_T interaction which includes the detector noise, the effects of previous crossings

(pile-up), the underlying event contributed by spectator partons to the high p_T interaction and the contribution from additional $p\bar{p}$ interactions. R_{jet} is a measure of the calorimeter energy response to jets due to e/π and energy losses in the calorimeter cracks. S compensates for the net energy flow through the jet cone boundary during the shower development in the calorimeter. The jet energy calibration is performed for several cone sizes, $\mathcal{R}$, from 0.3 to 1. Representative plots shown below are typically for central 0.7 cone jets.

2.3 Offset Correction

The total offset correction is measured as a transverse energy density in $\eta - \phi$ space and can be written as $D_O = D_{ue} + D_\theta$. The first term is the contribution from the physics underlying event, or the energy associated with the spectator partons. It is measured as the average transverse energy density in minimum bias events, which are dominated by hard core interactions. The second term accounts for the detector noise, pile-up effects, and energy from additional $p\bar{p}$ interactions. Pile-up increases with luminosity since it depends on the number of interactions in the previous crossing. D_θ is determined from a zero bias data sample, recorded on arbitrary beam crossings, which may or may not contain a hard interaction. The top plot in Fig. 7 shows the η dependence of D_{ue} for two center-of-mass energies 1800 and 630 GeV. D_{ue} is independent of the luminosity and the number of $p\bar{p}$ interactions in the event. The η and luminosity dependence of D_θ are shown in the bottom plot of Fig. 7.

2.4 Response and Showering Corrections

The overall calorimeter response to particles is less than unity. This is due to its non-linear response to low energy particles, inactive material, detector boundaries, and module-to-module non-uniformities. The $\gamma - jet$ data sample is a useful calibration tool in determining the calorimeter response to jets. These events consist of a photon balanced in p_T by one or more jets. For a $\gamma - jet$ event in the DØ detector, any non-zero E_T gives a measure of the overall transverse energy imbalance due to the differences in calorimeter response to photons and jets. In this case the jet response can be derived from

$$R_{jet} = 1 + \frac{\vec{\not\!\!E}_T \cdot \hat{n}_{T_\gamma}}{E_{T_\gamma}} \qquad (2)$$

where E_{T_γ} and $\hat{n}_{T_\gamma}$ are the transverse energy and direction of the photon, respectively.

R_{jet} includes η-dependent corrections arising from detector inhomogeneities and boundaries. Energy dependent corrections are also included to account for the jet

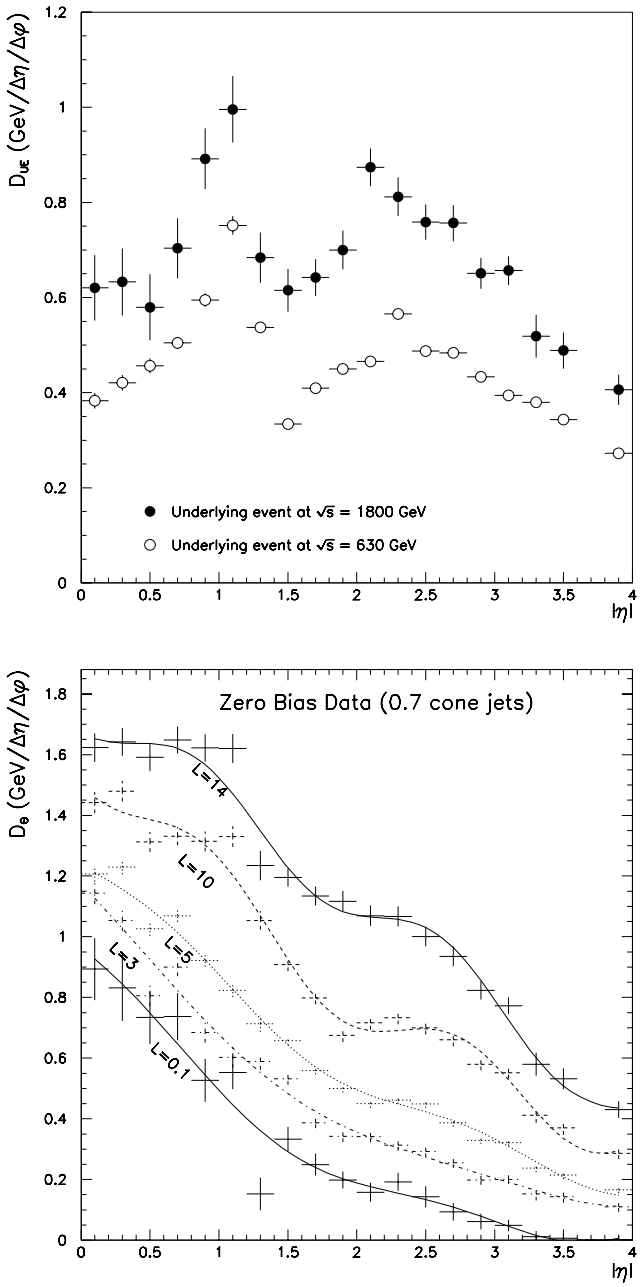

Figure 7: (Top) The underlying event density D_{ue} plotted as a function of η for the center-of-mass energies 1800 GeV and 630 GeV. (Bottom) The eta dependence of D_θ for different luminosities in units of $10^{30} cm^{-2} s{-}1$.

E_T threshold of 8 GeV, jet reconstruction inefficiencies and finite jet energy resolutions. The use of the CC data is limited to energies below 120 GeV due to the rapidly falling photon cross section. Data from the EC are used to extend the energy reach up to 300 GeV. Monte Carlo information is also included at high energy to constrain the jet energy response extrapolated from the data. The

variation of R_{jet} with the jet energy, shown in Fig. 8 for $\mathcal{R} = 0.7$ cone jets, is independent of the cone size and is the same for the 1800 GeV and 630 GeV data sets. The top plot is the same as the bottom plot except the jet energy axis is logarithmic to show the behavior of R_{jet} at low jet energies. The solid curve shown is a fit to the data with the associated error band. The fit has a functional form $R_{jet} = a + b \cdot \ln(E) + c \cdot \ln(E)^2$.

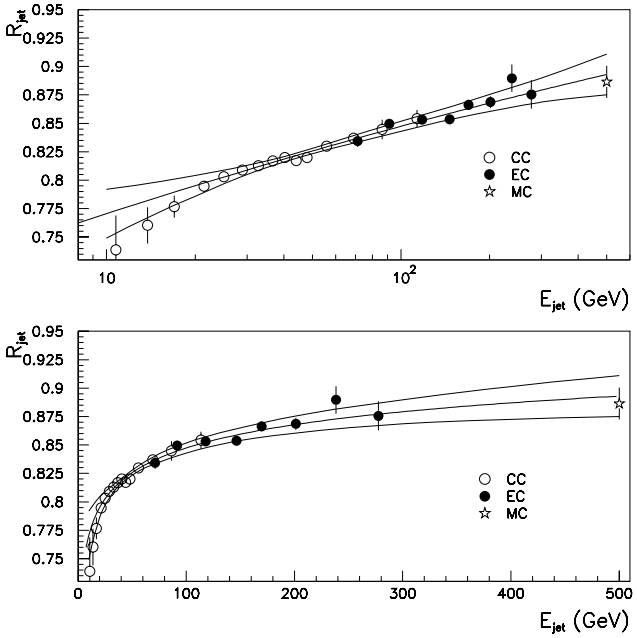

Figure 8: The dependence of R_{jet} on the jet energy, from the data using the central (CC) and end (EC) calorimeters, with 0.7 cone jets. The solid curve is the fit with the associated error band.

The last jet energy correction applied corrects for the effects of showering. It compensates for the energy associated with particles emitted inside the cone but deposited outside the cone as the shower develops. S is less than one which implies that the effect of showering is a net flow of energy from inside to outside the cone. The energy outside the cone may be associated with jet fragmentation outside the cone or gluon radiation. It may also be attributed to detector noise, pile-up and underlying event. The out-of-cone jet energy from gluon radiation and fragmentation effects, determined using the HERWIG [8] Monte Carlo at particle-level, is subtracted from the out-of-cone jet energy measured in the data. Showering losses are derived using jet energy density profiles using both the data and particle-level Monte Carlo. These losses have been shown [6] to have a strong dependence on the jet cone size $\mathcal{R}$, the jet energy, and η. They are independent of the center-of-mass energy for jets of the same energy and pseudorapidity.

2.5 Total Jet Energy Correction Factor

Figure 9 shows the total jet energy correction and the associated uncertainties as a function of the uncorrected jet energy for $|\eta| = 0$. The overall correction factor in the central calorimeter is 1.16 ± 0.015 and 1.12 ± 0.023 at 70 and 400 GeV, respectively. In general, the correction factors are about 15% above 30 GeV and almost flat all the way to E_T of 200 GeV. At lower jet energies, smaller cone sizes, and larger pseudorapidities, the corrections and errors increase. The total error is dominated by the contribution from showering corrections at large values of η.

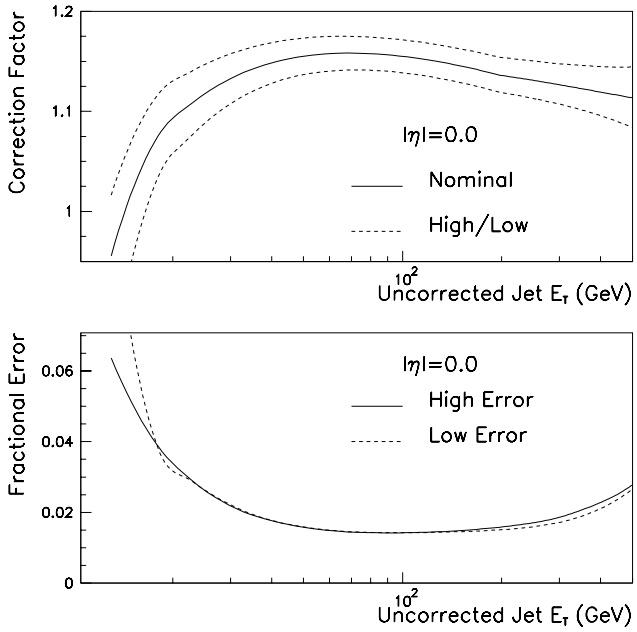

Figure 9: The total jet energy correction and associated errors versus the uncorrected jet energy.

3 Summary

The DØ experiment has performed a detailed evaluation of the jet energy scale based primarily on data taken during the 1992-1996 $p\bar{p}$ collider run at center-of-mass energies $\sqrt{s} = 1800\ GeV$ and 630 GeV. The energy corrections compensate for spectator interactions, detector noise, calorimeter response, and showering losses for the transverse energy and pseudorapidity range $E_T > 8\ GeV$ and $|\eta| < 3$. The correction procedure has been verified, using a HERWIG Monte Carlo sample with the full DØ detector simulation, which shows that the jet energy is corrected to the particle-level within the quoted errors.

This report also presented a general overview of the DØ upgrade. All aspects of the upgrade are well underway with many detector components moving into the production and construction stages. The upgraded DØ detector is scheduled to be complete by the spring of the year 2000.

References

1. DØ Collab., FERMILAB-PUB-96-357 (1996).
2. D. Adams *et al.*, IEEE Trans. Nucl. Sci. **43**, 1146 (1996).
3. DØ Collab., The DØ Silicon Tracker Technical Design Report, Fermilab (1995).
4. R. Yarema *et al.*, FERMILAB-TM-1892 (1994).
5. DØ Collab., *Nucl. Instrum. Methods* A **338**, 185 (1994).
6. DØ Collab., FERMILAB-PUB-97-330 (1998), submitted to *Nucl. Instrum. Methods* A.
7. J. Kotcher for the DØ Collab., FERMILAB-CONF-95-007 (1995).
8. G. Marchesini *et al.*, hep-ph/9607393 (1996).